symmetry

IMPACT FACTOR 2.940

CITESCORE 4.3

Article

Building an Equation of State Density Ladder

Marc Salinas and Jorge Piekarewicz

Special Issue

Symmetries and Ultra Dense Matter of Compact Stars

Edited by

Prof. Dr. Mannque Rho

MDPI

https://doi.org/10.3390/sym15050994

symmetry

MDPI

Article

Building an Equation of State Density Ladder

Marc Salinas * and Jorge Piekarewicz *

Department of Physics, Florida State University, Tallahassee, FL 32306, USA
* Correspondence: ms20lp@fsu.edu (M.S.); jpiekarewicz@fsu.edu (J.P.)

Abstract: The confluence of major theoretical, experimental, and observational advances are providing a unique perspective on the equation of state of dense neutron-rich matter—particularly its symmetry energy—and its imprint on the mass-radius relation for neutron stars. In this contribution, we organize these developments in an equation of the state density ladder. Of particular relevance to this discussion are the impact of the various rungs on the equation of state and the identification of possible discrepancies among the various methods. A preliminary analysis identifies possible tension between laboratory measurements and gravitational-wave detections that could indicate the emergence of a phase transition in the stellar core.

Keywords: neutron stars; equation of state; density functional theory

1. Introduction

What are the new states of matter that emerge at exceedingly high density and temperature? was featured among one of the "Eleven Science Questions for the New Century" posed by the Committee on the Physics of the Universe at the turn of the past century [1]. Closely related to this question and one at the center of nuclear science today is, *How does subatomic matter organize itself and what phenomena emerge?* [2]. Isolated neutron stars are ideal cosmic laboratories to study the emergence of new states of matter over an enormous range of densities spanning more than 10 orders of magnitude.

Neutron stars are cold, fully catalyzed astronomical objects that settle into the absolute ground state at the appropriate baryon density. In this manner, neutron stars provide a unique laboratory where a density can be dialed and the ground state of the system at such density explored. Moreover, being bound by gravity and not by the strong force conditions found in the neutron-star interior are impossible to reproduce in terrestrial laboratories.

Powerful insights into the structure, dynamics, and composition of neutron stars have emerged during the last few years from discoveries that probe different regions of the stellar interior. Given the confluence of such discoveries, it is fitting to introduce an "equation of state density ladder" [3], akin to the cosmic distance ladder used in cosmology, to illustrate the different techniques that are being used to probe the various regions of the neutron star. In this manner, each rung in the ladder represents a theoretical, experimental, or observational technique that determines the equation of state (EOS) in a suitable density regime. Paraphrasing from the cosmic distance ladder, no one method can determine the EOS over the entire density domain existent in a neutron star. Rather, each rung on the ladder informs the EOS of a density regime that can be connected to its neighboring rungs. Such a density ladder has been constructed in Figure 1 using a variety of theoretical, experimental, and observational methods that have propelled the field to a golden era of neutron stars [4,5]. In the next few sections, we will describe the remarkable progress made in these various arenas and examine their profound implication in constraining the equation of the state of dense matter.

Citation: Salinas, M.; Piekarewicz, J. Building an Equation of State Density Ladder. *Symmetry* **2023**, *15*, 994. https://doi.org/10.3390/sym15050994

Academic Editor: Mannque Rho

Received: 3 April 2023
Revised: 18 April 2023
Accepted: 19 April 2023
Published: 27 April 2023

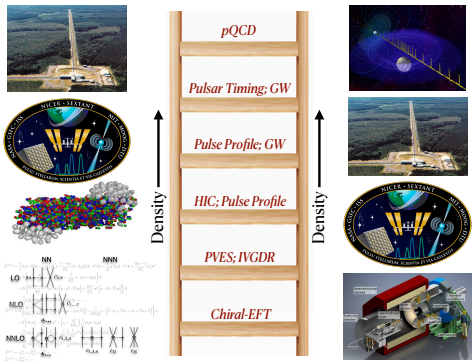

Figure 1. The equation of state density ladder. Each rung in the ladder represents a technique that informs the equation of the state of neutron-rich matter in a suitable density regime. With the exception of the isovector giant dipole resonance (IVGDR), Heavy Ion Collisions (HIC), and perturbative QCD (pQCD), the impact of all other methods on the EOS have been addressed in this contribution. Here GW stands for Gravitational Waves, and PVES for Parity-Violating Electron Scattering.

2. Chiral Effective Field Theory

The lowest rung in the density ladder displayed in Figure 1 is a purely theoretical approach developed by Steven Weinberg in the early 1990s. In a paper titled "Nuclear forces from chiral lagrangians" [6], Weinberg incorporated the approximate chiral symmetry of Quantum Chromodynamics into the construction of a nuclear Hamiltonian, where the long-range part of the interaction is mediated by the pion and the (unknown) short-range structure is encoded in contact interactions with empirical coefficients fitted to the data. Such a seminal paper has triggered a paradigm shift in theoretical nuclear physics. In essence, chiral effective field theory (χEFT) is a systematic, improvable, and quantifiable theoretical framework of nucleons interacting via the exchange of pions and unresolved short-range structure encoded in a few contact terms. Whereas χEFT combined with a variety of many-body methods have significantly advanced our understanding of the atomic nucleus—see, for example, Refs. [7–10] and references contained therein—in the present contribution, we focus on the impact χEFT has on our understanding of dense matter.

Given that nuclear matter saturates, namely, there is an equilibrium density of about $\rho_0 \approx 0.15\,\mathrm{fm}^{-3}$ that characterizes the interior density of medium to heavy nuclei, probing the nuclear dynamics below this density is particularly challenging. Chiral effective field theory offers the only realistic method to constrain the EOS below saturation density. Indeed, χEFT predictions of increasing quality and sophistication provide valuable insights into the EOS of pure neutron matter for densities below $1.5\rho_0$ [11–18]. We note that, as in the case of all effective field theories, χEFT includes a breakdown scale that defines the range of applicability of the theory. In the case of infinite nuclear matter, the approach is valid, provided the Fermi momentum is below the breakdown scale. It is precisely in this sense that no one method depicted in the density ladder can determine the EOS over the entire density domain.

Two quantities that will be used throughout this paper to compare the various approaches are the slope of the symmetry energy at saturation density (L) and the radius of a $1.4\,M_\odot$ neutron star. The symmetry energy quantifies the energy cost in turning symmetric nuclear matter into pure neutron matter and is defined as follows [19]:

$$S(\rho) = \frac{1}{2}\left(\frac{\partial^2 \varepsilon(\rho,\alpha)}{\partial \alpha^2}\right)_{\alpha=0}, \tag{1}$$

where $\varepsilon(\rho,\alpha)$ is the energy per nucleon of infinite nuclear matter that depends on the sum and difference of proton and neutron densities; that is, $\rho \equiv \rho_p + \rho_n$ and $\alpha \equiv (\rho_p - \rho_n)/\rho$, respectively. Note that infinite nuclear matter is an idealized system of neutrons and protons interacting exclusively via the strong force, without contribution from the electromagnetic

or weak interactions. Moreover, it is often convenient to characterize the behavior of the symmetry energy around saturation density in terms of a few bulk parameters, namely [19],

$$S(\rho) = J + L\,x + \frac{1}{2}K_{\rm sym}\,x^2 + \ldots \quad x \equiv \frac{(\rho-\rho_0)}{3\rho_0}, \tag{2}$$

where J, L, and $K_{\rm sym}$ are the values of the symmetry energy, its slope, and curvature at saturation density. Given that the slope of the symmetry energy is closely related to the pressure of pure neutron matter at saturation density, namely,

$$P_0 = \frac{1}{3}\rho_0 L, \tag{3}$$

this quantity is of critical importance as it determines both the neutron skin of heavy nuclei [20–23] as well as the radius of low-mass neutron stars [24–26]. In particular, χEFT predicts a value for the slope of the symmetry energy of $L = (59.8 \pm 4.1)$ MeV at the 1σ level [15].

3. Parity-Violating Electron Scattering: The Neutron Skin Thickness of ^{208}Pb

More than three decades ago, Donnelly, Dubach, and Sick proposed the use of Parity-Violating Electron Scattering (PVES) as a clean and model-independent probe of neutron densities [27]. The interest in measuring the neutron distribution of heavy nuclei (specifically of ^{208}Pb) was rekindled because of the enormously successful experimental program developed at the Thomas Jefferson National Accelerator Facility (Jefferson Lab) and by the impact that such a measurement could have in constraining the equation of the state of neutron-rich matter and ultimately the structure of neutron stars [24,25].

The parity-violating asymmetry is defined as the difference relative to the sum of the differential cross section for the elastic scattering of right-/left-handed longitudinally polarized electrons. In a simple plane-wave impulse approximation, the asymmetry emerges from the interference between two Feynman diagrams, a large one involving the exchange of a photon and a much smaller one involving the exchange of a Z^0 boson. As such, the parity-violating asymmetry becomes

$$\begin{aligned} A_{PV}(Q^2) &= \frac{\left(\frac{d\sigma}{d\Omega}\right)_R - \left(\frac{d\sigma}{d\Omega}\right)_L}{\left(\frac{d\sigma}{d\Omega}\right)_R + \left(\frac{d\sigma}{d\Omega}\right)_L}, \\ &= \frac{G_F Q^2}{4\pi\alpha\sqrt{2}}\frac{Q_{\rm wk}F_{\rm wk}(Q^2)}{ZF_{ch}(Q^2)}. \end{aligned} \tag{4}$$

where Q^2 is the square of four momentum transfer to the nucleus, α is the fine-structure constant, and G_F is the Fermi constant. In turn, the nuclear information is contained in the electric charge of the nucleus Z, its weak-vector charge $Q_{\rm wk} = -N + (1 - 4\sin^2\theta_{\rm W})Z$, and two form factors $F_{\rm wk}$ and F_{ch}, both normalized to one at $Q^2 = 0$. First, we note that because the weak charge of the proton is small, most of the weak charges of the nucleus is carried by the neutrons. Second, the two nuclear form factors are proportional to the Fourier transform of their respective densities. Finally, given that the charge form factor for a great number of nuclei is known with enormous precision [28], the one remaining unknown in the problem is $F_{\rm wk}$. Because the weak charge of the nucleus resides largely on the neutrons, the parity- violating asymmetry—as first suggested in Ref. [27]—provides an ideal, model-independent experimental tool to determine neutron densities.

Although it took decades since first suggested by Donnelly, Dubach, and Sick, the Lead Radius EXperiment (PREX) at Jefferson Lab fulfilled its promise to determine the neutron radius of ^{208}Pb with a precision of nearly 1% [29–31]. In particular, the neutron

skin thickness of ^{208}Pb—defined as the difference between the neutron and proton root-mean-square radii—was reported at the 1σ level to be [31]:

$$R_{\rm skin} = R_n - R_p = (0.283 \pm 0.071)\ {\rm fm}. \tag{5}$$

Although the error is large, the central value is much larger than previously anticipated, both by previous experimental and theoretical estimates [32,33]. Indeed, by relying on the strong correlation between the neutron skin thickness of ^{208}Pb and the slope of the symmetry energy, a value of $L = (106 \pm 37)$ MeV was obtained [32,33]. In turn, the large value of L implies a correspondingly large value for the radius of a $1.4\,M_\odot$ neutron star of $13.25 \lesssim R_{1.4}({\rm km}) \lesssim 14.26$, suggesting that the symmetry energy is fairly stiff [33]. It is worth noting that the extraction of L from the PREX experiment is significantly larger than the χEFT prediction of $L = (59.8\ \pm\ 4.1)$ MeV.

It has been argued that such a discrepancy may just be a statistical fluctuation, given that the two values agree at the 2σ level. At present, the only possibility of resolving whether the tension is real is at the future Mainz Energy-recovery Superconducting Accelerator (MESA) that is under construction at the Johannes Gutenberg University in Mainz, Germany [34]. If the Mainz Radius EXperiment (MREX) becomes feasible, one can anticipate a factor-of-two improvement in the determination of the neutron radius of ^{208}Pb relative to PREX.

4. LIGO-Virgo: Neutron Star Mergers

The historic detection of gravitational waves emitted from the binary neutron star merger GW170817 is providing fundamental new insights into the nature of dense matter [35]. Of great relevance to the equation of state are the so-called "chirp mass" and "chirp tidal deformability" (or simply $\tilde{\Lambda}$) given, respectively, by

$$\mathcal{M} = \frac{(M_1 M_2)^{3/5}}{(M_1 + M_2)^{1/5}}, \tag{6a}$$

$$\tilde{\Lambda} = \frac{16}{13}\frac{(M_1 + 12M_2)M_1^4\Lambda_1 + (M_2 + 12M_2)M_2^4\Lambda_2}{(M_1 + M_2)^5}, \tag{6b}$$

where the dimensionless tidal deformability of an individual neutron star of mass M and radius R is defined as [36–42].

$$\Lambda = \frac{2}{3}k_2\left(\frac{c^2 R}{GM}\right)^5 = \frac{64}{3}k_2\left(\frac{R}{R_s}\right)^5. \tag{7}$$

Here k_2 is the second Love number that is mildly sensitive to the equation of state, and R_s is the Schwarzschild radius of the neutron star. Note that for the equal mass case, $\tilde{\Lambda} = \Lambda_1 = \Lambda_2$. The tidal deformability is extremely sensitive to the equation of state as it scales as the fifth power of the compactness parameter M/R. The tidal field of the companion star induces a mass quadrupole moment in the neutron star that—in the linear regime—is proportional to the tidal field; the constant of proportionality is the tidal deformability. Thus, for a given mass, a larger (more "fluffy") neutron star is easier to tidally deform than a corresponding smaller star.

Whereas the chirp mass of GW170817 was determined with enormous precision (about a few parts in a thousand), the tidal deformability hides behind the fifth post-Newtonian coefficient in the waveform. Therefore, at the time of the discovery paper, only an upper bound on $\tilde{\Lambda}$ was reported [35]. Yet in a follow-up paper [43], the LIGO-Virgo collaboration was able to quote a value for the dimensionless tidal deformability of a $1.4\,M_\odot$ neutron star of $\Lambda_{1.4} = 190^{+390}_{-120}$, favoring soft EOSs, namely, those equations of state for which the pressure increases slowly with increasing density. In turn, soft equations of state predict compact stars with relatively small stellar radii.

5. NICER: Simultaneous Determination of Masses and Radii of Neutron Stars

Besides the tidal deformability, electromagnetic emissions from stellar hot spots are also highly sensitive to the compactness parameter. The Neutron Star Interior Composition Explorer (NICER) monitors soft X-rays emitted from stellar hot spots by relying on the powerful technique of Pulse Profile Modeling [44,45]. As the neutron star spins, traditional Newtonian gravity predicts an oscillating profile with no electromagnetic detection once the hot spots move away from the line of sight. However, one of the hallmarks of general relativity is gravitational light bending. This implies that the X-ray emissions, while modulated, may never completely disappear; NICER can "see" the back of the star. As gravitational light bending increases with increasing compactness M/R, a precise determination of the X-ray profile provides critical information on the EOS.

Remarkably, prior to the deployment of NICER in 2017, no systematic approach existed for the simultaneous determination of the mass and radius of a neutron star, even though the first pulsar was detected by Jocelyn Bell back in 1967 [46]. An early attempt at determining both the mass and radius of Hercules X-1 (Her X-1) was made by Leahy in 2004 [47]. By modeling the observed pulse shape of Her X-1, a constraint on the mass-radius ratio was obtained. That, in combination with a mass determination from the orbit, constrains a narrow region in the M-R plane, which excludes stiff equations of state. In the case of NICER, the first mass-radius determination focused on the millisecond pulsar PSR J0030+0451, with a mass in the neighborhood of the "canonical" mass of about 1.4 $M_\odot$ [48,49]. The second target of the NICER mission was the millisecond pulsar PSR J0740+6620 [50,51]. Although fainter than PSR J0030+0451, the great advantage of PSR J0740+6620 was that its mass was already known. Indeed, as discussed in Section 6, with a mass in excess of two solar masses, PSR J0740+6620 is currently the heaviest well-measured neutron star [52,53]. It is interesting to note that the stellar radii of both PSR J0030+0451 and PSR J0740+6620 are very close to each other; about 12.4 km. This result seems to validate a conjecture that suggests that neutron stars have approximately the same radius over a wide range of masses [54]. Moreover, that the radius is relatively large implies—unlike GW170817—that the equation of state is relatively stiff. Whereas this may indicate a mild tension, the error bars are currently too large to make a definite statement.

6. Pulsar Timing: Determination of the Most Massive Neutron Stars

The most stringent constraints on the high-density component of the EOS are placed by the most massive neutron stars. Unlike stellar radii that are sensitive to the EOS in the vicinity of twice saturation density, massive neutron stars inform the EOS at the highest densities achieved in the core. In particular, PSR J0740+6620 with a mass of $M = 2.08 \pm 0.07\, M_\odot$ has, until recently, been identified as the most massive neutron star to date [52,53]. The massive pulsar was detected by the Green Bank Telescope using Shapiro delay [55], often regarded as the fourth test of general relativity. The main concept behind Shapiro delay is that the electromagnetic radiation emitted by the neutron star experiences a time delay as it "dips" into the gravitational well induced by its white-dwarf companion on its way to the detector; no such delay exists when the neutron star is between the white dwarf and the observer. By accounting for every orbital period over long periods of time, pulsar timing provides a highly precise value for the mass of the white-dwarf star. Now using Kepler's third law of planetary motion, which is only sensitive to the sum of the individual masses, one can then extract the mass of PSR J0740+6620.

The record for the most massive neutron star was broken last year with the measurement of the mass of the black widow pulsar PSR J0952-0607. As part of a binary system with a faint sub-solar mass companion, the mass of PSR J0952-0607 was determined to be $M = 2.35 \pm 0.17\, M_\odot$ [56], a value that is likely to be near the upper limit for non-rotating neutron stars. Indeed, an analysis of GW190814—a gravitational wave detection from the coalescence of a 23 $M_\odot$ black hole with a 2.6 $M_\odot$ compact object, seems to suggest that GW190814 is unlikely to originate in a neutron star-black hole coalescence [57]. Such a claim is validated by an analysis of the ejecta during the spin-down phase of GW170817,

which places an upper limit on the maximum neutron star mass at $M_{\rm max} \lesssim 2.17\, M_\odot$ [58]. Regardless of the precise value of the maximum neutron star mass, it is clear that the EOS at the highest densities found in the stellar core must be stiff.

7. Results

In this section, we collect the theoretical, experimental, and observational information presented in the previous sections, and depicted on the EOS density ladder of Figure 1, to discuss the new set of energy density functionals introduced in Ref. [59] and its impact on the mass-radius relation.

To describe the nuclear dynamics and calculate ground states properties of finite nuclei, we employ the following effective interacting Lagrangian [24,60–64]:

$$\begin{aligned}\mathscr{L}_{\rm int} = \; & \bar{\psi}\Big[g_{\rm s}\phi - \Big(g_{\rm v}V_\mu + \frac{g_\rho}{2}\boldsymbol{\tau}\cdot\mathbf{b}_\mu + \frac{e}{2}(1+\tau_3)A_\mu\Big)\gamma^\mu\Big]\psi \\ & - \frac{\kappa}{3!}(g_{\rm s}\phi)^3 - \frac{\lambda}{4!}(g_{\rm s}\phi)^4 + \frac{\zeta}{4!}g_{\rm v}^4(V_\mu V^\mu)^2 \\ & + \Lambda_{\rm v}\Big(g_\rho^2\,\mathbf{b}_\mu\cdot\mathbf{b}^\mu\Big)\Big(g_{\rm v}^2 V_\nu V^\nu\Big)\,,\end{aligned} \tag{8}$$

where ψ is the isodoublet nucleon field, A_μ is the photon field, and ϕ, V_μ, and $\mathbf{b}_\mu$ represent the isoscalar-scalar σ-meson, the isoscalar-vector ω-meson, and the isovector-vector ρ-meson fields, respectively. The σ-meson is responsible for the intermediate range attraction of the nuclear force, the ω-meson mediates the repulsion at short distances, while the ρ-meson induces an isospin dependence that significantly impacts the nuclear symmetry energy.

For spatially non-uniform systems, we use the Kohn–Sham equations developed in the framework of density functional theory [65,66], which closely resemble a mean-field-like approach. For spherically symmetric nuclei, we solve the resulting sets of meson and nucleon field equations self consistently; see [67] and references contained therein. For a given nucleus, the observables obtained from such a self-consistent procedure are the binding energy per nucleon, the single-particle energies and associated Dirac orbitals, the resulting meson fields, and proton and neutron densities. In turn, by appropriately folding the proton and neutron densities with single-nucleon form factors determined experimentally, one can predict charge and weak-charge densities [68]. Particularly relevant to this work are proton, neutron, charge, and weak charge radii. In the particular case of the charge radius, this is obtained as follows:

$$R_{\rm ch}^2 = \frac{1}{Z}\int r^2\rho_{\rm ch}(r)d^3r = \frac{4\pi}{Z}\int_0^\infty r^4\rho_{\rm ch}(r)dr, \tag{9}$$

where we have used the spherical symmetry of the ground-state densities. Similar expressions may be written for the proton, neutron, and weak charge radii. Finally, given their importance in constraining the slope of the symmetry energy L, we define neutron skins and weak skins [68] by

$$R_{\rm nskin} = R_n - R_p, \tag{10a}$$

$$R_{\rm wskin} = R_{wk} - R_{ch}. \tag{10b}$$

For a given set of coupling constants and meson masses, $\mathbf{C} = \{m_{\rm s}, m_{\rm v}, m_\rho, g_{\rm s}, g_{\rm v}, g_\rho, \kappa, \lambda, \zeta, \Lambda_{\rm v}\}$, which we treat as the parameters of the model, we can obtain both properties of finite nuclei and the EOS for neutron star matter (NSM). Table 1 contains the four different sets of parameters that are used in this paper. The first two sets, FSUGold2 and FSUGarnet, were calibrated to properties of finite nuclei, such as binding energies, charge radii, and giant monopole resonances (GMR) [69,70]. The last two sets of parameters denote a recently refined version of the two models mentioned above. In this "re-calibration" of the models, input from χEFT, mass-radius measurements from NICER, and tidal deformability from

LIGO-Virgo, were used in a Bayesian framework to provide updated sets of coupling constants. More information on this method can be found in [59].

Table 1. Central values for the model parameters FSUGold2 and FSUGarnet before and after Bayesian refinement. The parameter κ and the meson masses m_s, m_v, and m_ρ are all given in MeV, and the nucleon mass has been fixed at $M = 939$ MeV.

Model	m_s	m_v	m_ρ	g_s^2	g_v^2	g_ρ^2	κ	λ	ζ	Λ_v
FSUGold2	497.479	782.500	763.000	108.094	183.789	80.466	3.0029	−0.000533	0.025600	0.000823
FSUGarnet	496.939	782.500	763.000	110.349	187.695	192.927	3.2600	−0.003551	0.023500	0.043377
FSUGold2+R	501.611	782.500	763.000	103.760	169.410	128.301	3.7924	−0.010635	0.011660	0.031621
FSUGarnet+R	495.633	782.500	763.000	109.130	186.481	142.966	3.2593	−0.003285	0.023812	0.038274

Starting at the lowest rung of the density ladder, we indicated earlier that χEFT favors a fairly soft EOS for pure neutron matter, which according to Equation (3) suggests that the symmetry energy in the vicinity of saturation density is also soft. As we now show, such a softening creates a mild tension when confronted against the second rung in the density ladder, namely, the Parity-Violating Electron Scattering experiment on ^{208}Pb carried out at Jefferson Lab [31]. As already alluded to, the slope of the symmetry energy L is highly correlated to the neutron skin thickness of ^{208} Pb [20–23]. The experimental value extracted from PREX and listed in Table 2 suggests an estimate for the slope of the symmetry energy $L = (106 \pm 37)$ MeV [33] that is significantly larger than the $L = (59.8 \pm 4.1)$ MeV prediction from χEFT [15]. Yet, as indicated in Table 2 and Figure 2, the large value of the neutron skin thickness extracted from PREX is in excellent agreement with the predictions from FSUGold2 prior to the refinement. Yet the impact of χEFT on the refinement of the functional is dramatic; the neutron skin thickness of ^{208}Pb goes down from the experimental value of $R^{208}_{\rm nskin} = 0.285$ fm to $R^{208}_{\rm nskin} = 0.203$ fm. Note, however, that due to the large experimental uncertainty, such a small value is not yet ruled out. Hence the need for a more precise determination of $R^{208}_{\rm nskin}$ at the future Mainz facility is well motivated.

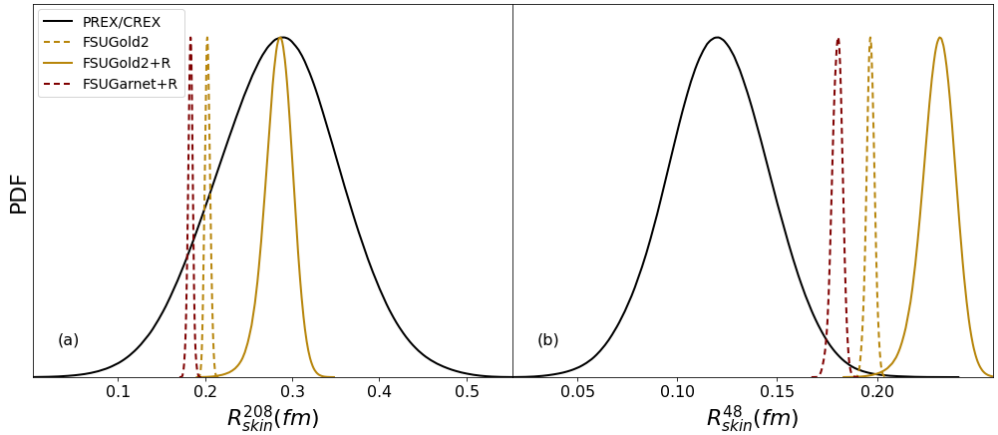

Figure 2. Posterior probability distribution functions (un-normalized) for the neutron skin thickness of (**a**) ^{208}Pb and (**b**) ^{48}Ca predicted by three of the models listed in Table 1 are compared with the corresponding experimental result from PREX [31] and CREX [71], respectively.

In Table 2 and Figure 2, we also compare our predictions for the neutron skin thickness of ^{48}Ca against the recently completed Calcium Radius EXperiment (CREX) [71]. Although as a medium mass nuclei, the correlation between L and $R^{48}_{\rm nskin}$ is, in general, not as strong as for ^{208}Pb [72], the class of covariant density functionals used in this work—and indeed most theoretical frameworks—suggest a fairly strong correlation between $R^{48}_{\rm nskin}$ and $R^{208}_{\rm nskin}$ [73]. Hence, it came as a surprise that $R^{48}_{\rm nskin}$ is significantly smaller than $R^{208}_{\rm nskin}$. For this case, the

impact of χEFT moves the FSUGold2 predictions in the right direction, but not nearly as much as required by CREX. At present, we are not aware of any theoretical approach that can simultaneously reproduce both the thick neutron skin in ^{208}Pb and the thin neutron skin in ^{48}Ca.

Table 2. Predictions from FSUGold2 before and after refinement (+R) for the charge radius, weak radius, weak skin, and neutron skin (all in fm) of ^{208}Pb and ^{48}Ca, as compared with the experimental values extracted from PREX [31] and CREX [71].

Model $(^{208}\mathbf{Pb})$	$R_{\mathbf{ch}}$	$R_{\mathbf{wk}}$	$R_{\mathbf{wskin}}$	$R_{\mathbf{nskin}}$
FSUGold2	5.491(6)	5.801(19)	0.310(16)	0.285(15)
FSUGold2+R	5.517(4)	5.743(05)	0.226(03)	0.203(03)
Experiment	5.501(1)	5.800(75)	0.299(75)	0.283(71)
Model $(^{48}\mathbf{Ca})$	$R_{\mathbf{ch}}$	$R_{\mathbf{wk}}$	$R_{\mathbf{wskin}}$	$R_{\mathbf{nskin}}$
FSUGold2	3.426(3)	3.707(07)	0.281(08)	0.231(08)
FSUGold2+R	3.477(8)	3.722(09)	0.245(02)	0.197(02)
Experiment	3.477(2)	3.636(35)	0.159(35)	0.121(35)

Besides constraints from χEFT that, as we just saw, have a strong impact on the refinement of the functionals, especially in the case of FSUGold2, our previous work also incorporated astrophysical constraints on the EOS of neutron star matter from the tidal deformability of GW170817 extracted by the LIGO-Virgo collaboration [35], stellar masses and radii of two sources obtained by the NICER mission [48–51], and lower limits on the maximum mass of a neutron star obtained from long-time pulsar timing observations [52,53]. Indeed, all this information—together with constraints on the EOS of pure neutron matter predicted by χEFT—was included in the model refinement [59]. By including all this new information in a Bayesian inference approach, posterior distribution functions were obtained for the neutron star matter EOS, the resulting mass-radius relation, and the tidal deformability of a 1.4 $M_{\odot}$ neutron star.

Ascending to the fourth rung in the density ladder, we now focus on the gravitational wave profile of GW170817 that, as we mentioned earlier, allows for the extraction of important structural observables, such as the chirp mass and tidal deformability. In Figure 3 we examine the model predictions for the tidal deformability of a 1.4 $M_{\odot}$ neutron star against the recommended value extracted by the LIGO-Virgo collaboration of $\Lambda_{1.4} = 190^{+390}_{-120}$, with both the upper and lower limits indicating 90% confidence levels [43]. This comparison is quite striking as it indicates a significant softening of the EOS at intermediate densities that is not reflected in any of the models—even after refinement. If such a discrepancy persists after further scrutiny, see, for example, Ref. [74], this could indicate that the softening may be a reflection of a phase transition in the stellar interior.

We conclude this section by displaying the holy grail of neutron star structure—the mass-radius relationship—alongside the neutron star matter equation of state. Recall that there is a one-to-one correspondence between the EOS and the mass-radius relation [75], with the EOS providing the microscopic underpinning of the macroscopic manifestation. The left-hand panel in Figure 4 depicts the EOS of neutron star matter, namely, the EOS of charge-neutral, neutron-rich matter in beta equilibrium. Such a relation between the pressure and energy density is the sole ingredient required to solve the Tolman–Oppenheimer–Volkoff equations to generate the mass-radius relation. For reference, we note that a value for the energy density of about $\varepsilon \sim 500\,\mathrm{MeV/fm^3}$ corresponds to a baryon density of about three times nuclear matter saturation density. We also note that the refined models are consistent with the limits on stellar radii recommended by the NICER mission, depicted in the figure by the 68% and 95% confidence ellipses. Regardless of whether the softening suggested by the tidal deformability is confirmed, the EOS at the highest densities found in the core must be stiff enough to support neutron stars with a mass in excess of two solar

masses. Our results indicate that within a 2σ error, all of our models are consistent with the very large mass of PSR J0952-0607 [56].

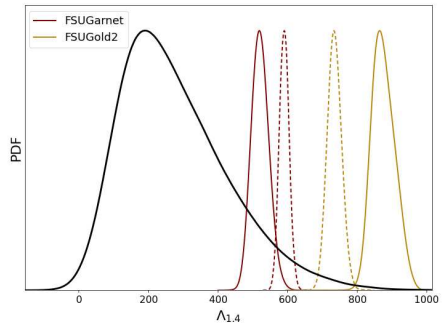

Figure 3. Tidal deformability measurement of a 1.4 $M_{\odot}$ neutron star [43] (black line) along with the predictions from FSUGold2 and FSUGarnet using their respective colors before and after refinement; the dashed curves indicate predictions post-refinement.

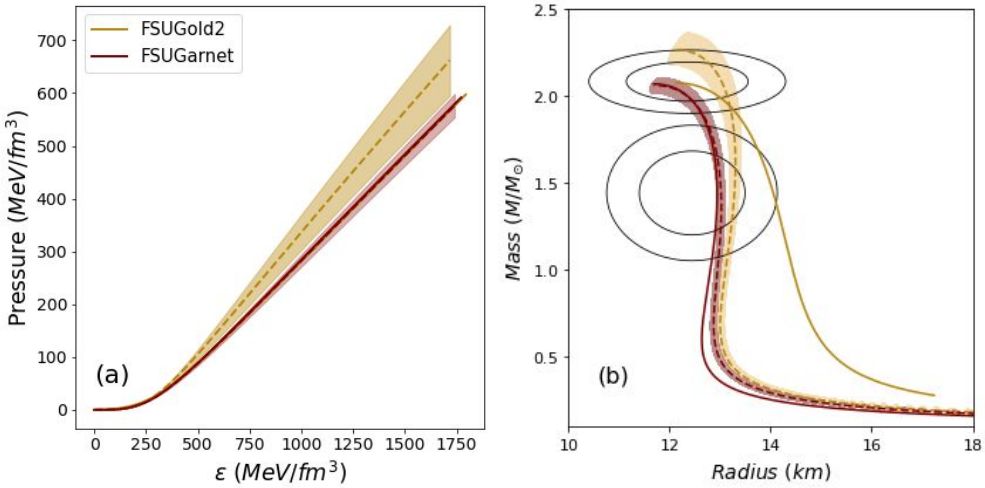

Figure 4. (**a**) Equation of state of neutron star matter as predicted by FSUGold2 [69], FSUGarnet [70], along with the results post-refinement [59]. (**b**) Mass-radius relationship predictions from FSUGold2 and FSUGarnet are displayed with their respective colors, with the solid and dashed lines representing results before and after Bayesian refinement, respectively. Theoretical error bands for FSUGold2 and FSUGarnet were computed at the 95% level, and the observational covariance ellipses (black) represent the 68% and 95% confidence intervals.

8. Conclusions

The confluence of major theoretical, experimental, and observational advances in our understanding of dense matter have motivated the creation of an equation of the state density ladder, where the various rungs in the ladder provide information at specific densities; no single rung can determine the EOS over the enormous density range spanned in a neutron star. Moreover, the range of densities probed by each rung in the ladder overlaps with neighboring rungs, thereby providing consistency checks among the various methods. Following our recent work [59], in which previously calibrated covariant energy density functionals were refined by the plethora of new information, we have examined the predictions of the new models.

First, we concluded that incorporating χEFT information significantly softens the previously stiff FSUGold2 energy density functional. Whereas such a softening shifts the FSUGold2+R predictions closer to CREX and LIGO-Virgo, the shift is not nearly as dramatic as the experiment and observation demand. Moreover, the previous excellent agreement with PREX is now lost. Both PREX and CREX will greatly benefit from more precise

measurements—which hopefully may be realized at the future Mainz Energy-recovery Superconducting Accelerator (MESA) [34]. In short, the original FSUGold2 prediction reproduces the PREX result but grossly overestimates the CREX value. As for the FSUGold2+R model, the softening of the EOS slightly shifts the result closer to the CREX extraction, but at the cost of losing agreement with PREX. This is the best compromise that can be achieved with the present set of covariant energy density functionals, suggesting that improvements to the isovector sector of the density functions are required. Regardless of the limiting set of models used in this contribution, we underscore that we are not aware of any theoretical approach that can simultaneously reproduce both CREX and PREX.

Besides χEFT, the extraction of the tidal deformability of a 1.4 $M_{\odot}$ [43] also disfavors a stiff EOS. As shown in this work, all model predictions fall on the high-end tail of the observational value. Given that both NICER and current values for the maximum mass neutron star require a fairly stiff EOS if confirmed, the softening suggested by LIGO-Virgo at intermediate densities may be an indication of a phase transition. At present, such a conclusion is premature, given that most of the observations have large statistical errors. However, given that we have just entered the golden era of neutron stars, the promise of significant advances in all areas of relevance to the EOS of dense matter is likely to bring unprecedented precision into the study of neutron stars.

Author Contributions: Conceptualization, M.S. and J.P.; Calculation and visualization M.S. and J.P.; Writing M.S. and J.P. All authors have read and agreed to the published version of the manuscript.

Funding: This material is based upon work supported by the U.S. Department of Energy Office of Science, Office of Nuclear Physics under Award Number DE-FG02-92ER40750.

Data Availability Statement: Not applicable.

Conflicts of Interest: The authors declare no conflict of interest.

References

1. *Connecting Quarks with the Cosmos: Eleven Science Questions for the New Century*; The National Academies Press: Washington, DC, USA, 2003.
2. Geesaman, D. Reaching for the horizon: The 2015 long range plan for nuclear science. *Nucl. Phys. News* **2015**, *26*, 3–4. [CrossRef]
3. Piekarewicz, J. The Nuclear Physics of Neutron Stars. *arXiv* **2022**, arXiv:2209.14877.
4. Baym, G. The Golden Era of Neutron Stars: From Hadrons to Quarks. *JPS Conf. Proc.* **2019**, *26*, 011001. [CrossRef]
5. Baym, G.; Hatsuda, T.; Kojo, T.; Powell, P.D.; Song, Y.; Takatsuka, T. From hadrons to quarks in neutron stars: A review. *Rept. Prog. Phys.* **2018**, *81*, 056902. [CrossRef] [PubMed]
6. Weinberg, S. Nuclear forces from chiral Lagrangians. *Phys. Lett. B* **1990**, *251*, 288–292 . [CrossRef]
7. Bedaque, P.F.; van Kolck, U. Effective field theory for few nucleon systems. *Ann. Rev. Nucl. Part. Sci.* **2002**, *52*, 339–396. [CrossRef]
8. Epelbaum, E.; Hammer, H.-W.; Meissner, U.-G. Modern Theory of Nuclear Forces. *Rev. Mod. Phys.* **2009**, *81*, 1773. [CrossRef]
9. Machleidt, R.; Entem, D.R. Chiral effective field theory and nuclear forces. *Phys. Rept.* **2011**, *503*, 1. [CrossRef]
10. Rodriguez Entem, D.; Machleidt, R.; Nosyk, Y. Nucleon-Nucleon Scattering Up to N5LO in Chiral Effective Field Theory. *Front. Phys.* **2020**, *8*, 57. [CrossRef]
11. Hebeler, K.; Schwenk, A. Chiral three-nucleon forces and neutron matter. *Phys. Rev.* **2010**, *C82*, 014314. [CrossRef]
12. Tews, I.; Kruger, T.; Hebeler, K.; Schwenk, A. Neutron matter at next-to-next-to-next-to-leading order in chiral effective field theory. *Phys. Rev. Lett.* **2013**, *110*, 032504. [CrossRef]
13. Kruger, T.; Tews, I.; Hebeler, K.; Schwenk, A. Neutron matter from chiral effective field theory interactions. *Phys. Rev.* **2013**, *C88*, 025802. [CrossRef]
14. Lonardoni, D.; Tews, I.; Gandolfi, S.; Carlson, J. Nuclear and neutron-star matter from local chiral interactions. *Phys. Rev. Res.* **2020**, *2*, 22033. [CrossRef]
15. Drischler, C.; Furnstahl, R.; Melendez, J.; Phillips, D. How Well Do We Know the Neutron-Matter Equation of State at the Densities Inside Neutron Stars? A Bayesian Approach with Correlated Uncertainties. *Phys. Rev. Lett.* **2020**, *125*, 202702. [CrossRef]
16. Drischler, C.; Holt, J.W.; Wellenhofer, C. Chiral Effective Field Theory and the High-Density Nuclear Equation of State. *Ann. Rev. Nucl. Part. Sci.* **2021**, *71*, 403. [CrossRef]
17. Sammarruca, F.; Millerson, R. Analysis of the neutron matter equation of state and the symmetry energy up to fourth order of chiral effective field theory. *Phys. Rev. C* **2021**, *104*, 034308. [CrossRef]
18. Sammarruca, F.; Millerson, R. The Equation of State of Neutron-Rich Matter at Fourth Order of Chiral Effective Field Theory and the Radius of a Medium-Mass Neutron Star. *Universe* **2022**, *8*, 133. [CrossRef]
19. Piekarewicz, J.; Centelles, M. Incompressibility of neutron-rich matter. *Phys. Rev.* **2009**, *C79*, 054311. [CrossRef]

20. Brown, B.A. Neutron radii in nuclei and the neutron equation of state. *Phys. Rev. Lett.* **2000**, *85*, 5296. [CrossRef]
21. Furnstahl, R.J. Neutron radii in mean-field models. *Nucl. Phys.* **2002**, *A706*, 85. [CrossRef]
22. Roca-Maza, X.; Centelles, M.; Viñas, X.; Warda, M. Neutron skin of ^{208}Pb, nuclear symmetry energy, and the parity radius experiment. *Phys. Rev. Lett.* **2011**, *106*, 252501. [CrossRef] [PubMed]
23. Piekarewicz, J.; Fattoyev, F.J. Neutron rich matter in heaven and on Earth. *Phys. Today* **2019** , *72*, 30. [CrossRef]
24. Horowitz, C.J.; Piekarewicz, J. Neutron star structure and the neutron radius of ^{208}pb. *Phys. Rev. Lett.* **2001**, *86*, 5647. [CrossRef]
25. Horowitz, C.J.; Piekarewicz, J. The neutron radii of lead and neutron stars. *Phys. Rev.* **2001**, *C64*, 062802.
26. Carriere, J.; Horowitz, C.J.; Piekarewicz, J. Low mass neutron stars and the equation of state of dense matter. *Astrophys. J.* **2003**, *593*, 463. [CrossRef]
27. Donnelly, T.; Dubach, J.; Sick, I. Isospin Dependencies in Parity Violating Electron Scattering. *Nucl. Phys.* **1989**, *A503*, 589. [CrossRef]
28. Angeli, I.; Marinova, K. Table of experimental nuclear ground state charge radii: An update. *At. Data Nucl. Data Tables* **2013**, *99*, 69. [CrossRef]
29. Abrahamyan, S.; Ahmed, Z.; Albataineh, H.; Aniol, K.; Armstrong, D.S.; Armstrong, W.; Averett, T.; Babineau, B.; Barbieri, A.; Bellini, V.; et al. Measurement of the Neutron Radius of ^{208}pb Through Parity-Violation in Electron Scattering. *Phys. Rev. Lett.* **2012**, *108*, 112502. [CrossRef]
30. Horowitz, C.J.; Ahmed, Z.; Jen, C.M.; Rakhman, A.; Souder, P.A.; Dalton, M.M.; Liyanage, N.; Paschke, K.D.; Saenboonruang, K.; Silwal, R.; et al. Weak charge form factor and radius of 208Pb through parity violation in electron scattering. *Phys. Rev.* **2012**, *C85*, 032501. [CrossRef]
31. Adhikari, D.; Albataineh, H.; Androic, D.; Aniol, K.; Armstrong, D.S.; Averett, T.; Barcus, S.; Bellini, V.; Beminiwattha, R.S.; Benesch, J.F.; et al. Accurate Determination of the Neutron Skin Thickness of ^{208}Pb through Parity-Violation in Electron Scattering. *Phys. Rev. Lett.* **2021**, *126*, 172502. [CrossRef]
32. Thiel, M.; Sfienti, C.; Piekarewicz, J.; Horowitz, C.J.; Vanderhaeghen, M. Neutron skins of atomic nuclei: per aspera ad astra. *J. Phys.* **2019**, *G46*, 093003. [CrossRef]
33. Reed, B.T.; Fattoyev, F.J.; Horowitz, C.J.; Piekarewicz, J. Implications of PREX-II on the equation of state of neutron-rich matter. *Phys. Rev. Lett.* **2021**, *126*, 172503. [CrossRef]
34. Becker, D.; Bucoveanu, R.; Grzesik, C.; Kempf, R.; Imai, K.; Molitor, M.; Tyukin, A.; Zimmermann, M.; Armstrong, D.; Aulenbacher, K.; et al. The P2 experiment. *Eur. Phys. J. A* **2018**, *54*, 208. [CrossRef]
35. Abbott, B.P.; Abbott, R.; Abbott, T.D.; Acernese, F.; Ackley, K.; Adams, C.; Adams, T.; Addesso, P.; Adhikari, R.X.; Adya, V.B.; et al. GW170817: Observation of Gravitational Waves from a Binary Neutron Star Inspiral. *Phys. Rev. Lett.* **2017**, *119*, 161101. [CrossRef]
36. Hinderer, T. Tidal Love numbers of neutron stars. *Astrophys. J.* **2008**, *677*, 1216. [CrossRef]
37. Hinderer, T.; Lackey, B.D.; Lang, R.N.; Read, J.S. Tidal deformability of neutron stars with realistic equations of state and their gravitational wave signatures in binary inspiral. *Phys. Rev.* **2010**, *D81*, 123016. [CrossRef]
38. Damour, T.; Nagar, A. Relativistic tidal properties of neutron stars. *Phys. Rev.* **2009**, *D80*, 84035. [CrossRef]
39. Postnikov, S.; Prakash, M.; Lattimer, J.M. Tidal Love Numbers of Neutron and Self-Bound Quark Stars. *Phys. Rev.* **2010**, *D82*, 24016. [CrossRef]
40. Fattoyev, F.J.; Carvajal, J.; Newton, W.G.; Li, B.-A. Constraining the high-density behavior of the nuclear symmetry energy with the tidal polarizability of neutron stars. *Phys. Rev.* **2013**, *C87*, 015806. [CrossRef]
41. Steiner, A.W.; Gandolfi, S.; Fattoyev, F.J.; Newton, W.G. Using Neutron Star Observations to Determine Crust Thicknesses, Moments of Inertia, and Tidal Deformabilities. *Phys. Rev.* **2015**, *C91*, 015804. [CrossRef]
42. Fattoyev, F.J.; Piekarewicz, J.; Horowitz, C.J. Neutron skins and neutron stars in the multi-messenger era. *Phys. Rev. Lett.* **2018**, *120*, 172702. [CrossRef] [PubMed]
43. Abbott, B.P.; Abbott, R.; Abbott, T.D.; Acernese, F.; Ackley, K.; Adams, C.; Adams, T.; Addesso, P.; Adhikari, R.X.; Adya, V.B.; et al. GW170817: Measurements of neutron star radii and equation of state. *Phys. Rev. Lett.* **2018**, *121*, 161101. [CrossRef] [PubMed]
44. Psaltis, D.; Özel, F.; Chakrabarty, D. Prospects for Measuring Neutron-Star Masses and Radii with X-ray Pulse Profile Modeling. *Astrophys. J.* **2014**, *787*, 136. [CrossRef]
45. Watts, A.L.; Andersson, N.; Chakrabarty, D.; Feroci, M.; Hebeler, K.; Israel, G.; Lamb, F.K.; Miller, M.C.; Morsink, S.; Ozel, F.; et al. Colloquium: Measuring the neutron star equation of state using x-ray timing. *Rev. Mod. Phys.* **2016**, *88*, 021001. [CrossRef]
46. Hewish, A.; Bell, S.; Pilkington, J.; Scott, P.; Collins, R. Observation of a Rapidly Pulsating Radio Source. *Nature* **1968**, *217*, 709. [CrossRef]
47. Leahy, D.A. Mass-radius constraints from a pulse shape model for hercules x-1. *Astrophys. J.* **2004**, *613*, 517. [CrossRef]
48. Riley, T.E.; Watts, A.L.; Bogdanov, S.; Ray, P.S.; Ludlam, R.M.; Guillot, S.; Arzoumanian, Z.; Baker, C.L.; Bilous, A.V.; Chakrabarty, D.; et al. A NICER View of PSR J0030+0451: Millisecond Pulsar Parameter Estimation. *Astrophys. J. Lett.* **2019**, *887*, L21. [CrossRef]
49. Miller, M.C.; Lamb, F.K.; Dittmann, A.J.; Bogdanov, S.; Arzoumanian, Z.; Gendreau, K.C.; Guillot, S.; Harding, A.K.; Ho, W.C.G.; Lattimer, J.M.; et al. PSR J0030+0451 Mass and Radius from NICER Data and Implications for the Properties of Neutron Star Matter. *Astrophys. J. Lett.* **2019**, *887*, L24. [CrossRef]
50. Riley, T.E.; Watts, A.L.; Ray, P.S.; Bogdanov, S.; Guillot, S.; Morsink, S.M.; Bilous, A.V.; Arzoumanian, Z.; Choudhury, D.; Deneva, J.S.; et al. A NICER View of the Massive Pulsar PSR J0740+6620 Informed by Radio Timing and XMM-Newton Spectroscopy. *Astrophys. J. Lett.* **2021** , *918*, L27. [CrossRef]

51. Miller, M.C.; Lamb, F.K.; Dittmann, A.J.; Bogdanov, S.; Arzoumanian, Z.; Gendreau, K.C.; Guillot, S.; Ho,W.C.G.; Lattimer, J.M.; Loewenstein, M.; et al. The Radius of PSR J0740+6620 from NICER and XMM-Newton Data. *Astrophys. J. Lett.* **2021**, *918*, L28. [CrossRef]
52. Cromartie, H.T.; Fonseca, E.; Ransom, S.M.; Demorest, P.B.; Arzoumanian, Z.; Blumer, H.; Brook, P.R.; DeCesar, M.E.; Dolch, T.; Ellis, J.A.; et al. Relativistic Shapiro delay measurements of an extremely massive millisecond pulsar. *Nat. Astron.* **2019**, *4*, 72. [CrossRef]
53. Fonseca , E.; Cromartie, H.T.; Pennucci, T.T.; Ray, P.S.; Kirichenko, A.Y.; Ransom, S.M.; Demorest, P.B.; Stairs, I.H.; Arzoumanian, Z.; Guillemot, L.; et al. Refined Mass and Geometric Measurements of the High-mass PSR J0740+6620. *Astrophys. J. Lett.* **2021**, *915*, L12. [CrossRef]
54. Guillot, S.; Servillat, M.; Webb, N.A.; Rutledge, R.E. Measurement of the Radius of Neutron Stars with High S/N Quiescent Low-mass X-ray Binaries in Globular Clusters. *Astrophys. J.* **2013**, *772*, 7. [CrossRef]
55. Shapiro, I.I. Fourth test of general relativity. *Phys. Rev. Lett.* **1964**, *13*, 789. [CrossRef]
56. Romani, R.W.; Kandel, D.; Filippenko, A.V.; Brink, T.G.; Zheng, W. PSR J0952−0607: The Fastest and Heaviest Known Galactic Neutron Star. *Astrophys. J. Lett.* **2022**, *934*, L18. [CrossRef]
57. Abbott, R.; Abbott, T.D.; Abraham, S.; Acernese, F.; Ackley, K.; Adams, C.; Adhikari, R.X.; Adya, V.B.; Affeldt, C.; Agathos, M.; et al. GW190814: Gravitational Waves from the Coalescence of a 23 Solar Mass Black Hole with a 2.6 Solar Mass Compact Object. *Astrophys. J.* **2020**, *896*, L44. [CrossRef]
58. Margalit, B.; Metzger, B.D. Constraining the Maximum Mass of Neutron Stars From Multi-Messenger Observations of GW170817. *Astrophys. J.* **2017**, *850*, L19. [CrossRef]
59. Salinas, M.; Piekarewicz, J. Bayesian refinement of covariant energy density functionals. *arXiv* **2023**, arXiv:2301.09692.
60. Walecka, J.D. A theory of highly condensed matter. *Ann. Phys.* **1974**, *83*, 491. [CrossRef]
61. Boguta, J.; Bodmer, A.R. Relativistic calculation of nuclear matter and the nuclear surface. *Nucl. Phys.* **1977**, *A292*, 413. [CrossRef]
62. Serot, B.D.; Walecka, J.D. The relativistic nuclear many body problem. *Adv. Nucl. Phys.* **1986**, *16*, 1.
63. Mueller, H.; Serot, B.D. Relativistic mean-field theory and the high-density nuclear equation of state. *Nucl. Phys.* **1996**, *A606*, 508. [CrossRef]
64. Serot, B.D.; Walecka, J.D. Recent progress in quantum hadrodynamics. *Int. J. Mod. Phys.* **1997**, *E6*, 515. [CrossRef]
65. Hohenberg, P.; Kohn, W. Inhomogeneous Electron Gas. *Phys. Rev.* **1964**, *136*, B864. [CrossRef]
66. Kohn, W.; Sham, L.J. Self-consistent equations including exchange and correlation effects. *Phys. Rev.* **1965**, *140*, A1133. [CrossRef]
67. Giuliani, P.; Godbey, K.; Bonilla, E.; Viens, F.; Piekarewicz, J. Bayes goes fast: Uncertainty Quantification for a Covariant Energy Density Functional emulated by the Reduced Basis Method. *Front. Phys.* **2023**, *10*, 1054524. [CrossRef]
68. Horowitz, C.J.; Piekarewicz, J. Impact of spin-orbit currents on the electroweak skin of neutron-rich nuclei. *Phys. Rev.* **2012**, C*86*, 045503. [CrossRef]
69. Chen, W.-C.; Piekarewicz, J. Building relativistic mean field models for finite nuclei and neutron stars. *Phys. Rev.* **2014**, *C90*, 044305. [CrossRef]
70. Chen, W.-C.; Piekarewicz, J. Searching for isovector signatures in the neutron-rich oxygen and calcium isotopes. *Phys. Lett.* **2015**, *B*748, 284. [CrossRef]
71. Adhikari, D.; Albataineh, H.; Androic, D.; Aniol, K.A.; Armstrong, D.S.; Averett, T.; Ayerbe Gayoso, C.; Barcus, S.K.; Bellini, V.; Beminiwattha, R.S.; et al. Precision Determination of the Neutral Weak Form Factor of Ca48. *Phys. Rev. Lett.* **2022**, *129*, 042501. [CrossRef]
72. Piekarewicz, J.; Agrawal, B.; Colò, G.; Nazarewicz, W.; Paar, N.; Reinhard, P.G.; Roca-Maza, X.; Vretenar, D. Electric dipole polarizability and the neutron skin. *Phys. Rev.* **2012**, *C85*, 041302(R). [CrossRef]
73. Piekarewicz, J. Implications of PREX-2 on the electric dipole polarizability of neutron-rich nuclei. *Phys. Rev. C* **2021**, 104, 024329. [CrossRef]
74. Gamba, R.; Breschi, M.; Bernuzzi, S.; Agathos, M.; Nagar, A. Waveform systematics in the gravitational-wave inference of tidal parameters and equation of state from binary neutron star signals. *Phys. Rev. D* **2021**, *103*, 124015. [CrossRef]
75. Lindblom, L. Determining the nuclear equation of state from neutron-star masses and radii. *Astrophys. J.* **1992**, 398, 569. [CrossRef]